Viscoelastic Properties of Cells: Modeling and Identification by Atomic Force Microscopy

Michael R. P. Ragazzon*, J. Tommy Gravdahl

Department of Engineering Cybernetics, NTNU, Norwegian University of Science and Technology, Trondheim, Norway.

Marialena Vagia

SINTEF ICT, Applied Cybernetics, Trondheim, Norway.

Abstract

Identification of mechanical properties of cells has previously been shown to have a great potential and effectiveness on medical diagnosis. As a result, it has gathered increasing interest of researchers over the recent years. Atomic force microscopy has become one of the prime technologies for obtaining such properties. Traditionally, local variations in elasticity has been obtained by mapping contact force during sample indentation to static Hertzian contact models. More recently, multiharmonic methods have allowed for both viscous and elastic measurements of soft samples. In this article, a new technique is presented based on dynamic modeling and identification of the sample. Essentially, the measured signals are mapped to the sample properties of the model in a least-square sense. This approach allows for easy extensibility beyond pure viscoelastic measurements. Furthermore, an iterative modeling approach can be used to best describe the measured data. The technique can be operated in either dynamic indentation viscoelastic mode, or scanning viscoelastic mode. First, a dynamic, viscoelastic model of the sample is presented. Then, the parameter identification method is described, showing exponential convergence of the parameters. A simulation study demonstrates the effectiveness of the approach in both modes of operation.

Keywords: mechanical properties, biomedical systems, parameter identification, dynamic models, atomic force microscopy

1. Introduction

Since its invention in 1986, atomic force microscopy (AFM) has become one of the leading technologies for imaging sample surfaces at nanometer scale resolutions [1]. In the beginning, AFM was applied almost exclusively to characterize the surfaces of nonbiological materials [2], and even today, its major applications are still in the visualization of microcircuits, material sciences and nanotechnology [3]. However, application of AFM to biological and biomedical research has increased exponentially during the recent years [4], since the AFM enjoys several advantages over conventional optical microscopes and electron microscopes, especially concerning studies of biological samples [1].

The main beneficial feature of AFM in the study of biological samples is its ability to study the objects directly in their natural conditions. Other advantages include: [5] 1) AFM can get information about surfaces in situ and in vitro, if not in vivo, in air, in water, buffers and other ambient media, 2) it has an extremely high scanning resolution, up to nanometer (molecular) resolution, and up to 0.01 nm vertical resolution, 3) it provides true 3D surface topographical information, 4) it can scan with a wide range of forces, starting from virtually zero to large destructive forces, 5) it allows measuring various biophysical properties of materials including elasticity, adhesion, hardness, and friction.

In order to improve early diagnosis of cancer there is an urgent need to increase understanding of cancer biology on a cellular level. Single cell deformability has been studied for a long time using various techniques. The driving force for such studies is the assumption that, depending on disease type, the altered cellular deformability should play a critical role in the development and progression of various diseases [6]. So far, several approaches have been investigated, including methods such as micro-pipette manipulation [7], magnetic bead twisting [8], and optical tweezers [9]. With these techniques, local variations in the viscoelastic power law parameters have been observed [10].

AFM has enjoyed many improvements to its main capa-

*Corresponding author

Email address: michael.remo.ragazzon@ntnu.no (Michael R. P. Ragazzon)

bilities from a control engineering point of view [11, 12, 13, 14, 15, 16, 17, 18]. Additionally, effort has been put into trying to discover the potential of AFM in cancer detection [1, 19, 6, 20, 5, 21, 22, 10, 23]. Any research result that would provide the possibility of an early and easy diagnosis of carcinoid cells with accuracy is of extreme interest to specialists that deal with the diagnosis and cure of the disease. In [24] AFM measurements of the human breast biopsies reveal unique mechanical fingerprints that help define the stages of cancer progression. High-resolution stiffness mapping shows that in addition to matrix stiffening, tumor progression is due to softening of the tumor cells.

Clearly, mechanical properties of cells are of high interest to the research community. The elastic modulus of biological samples are typically found through force-indentation procedures [25, 26], performed statically. That is, by indenting the sample and measuring the deflection against the commanded cantilever position. By fitting the resulting curve to the Hertz contact model, the elastic modulus of the sample can be determined. Furthermore, extensions to the Hertz model allow for determining the adhesion between the tip and sample from the force-distance curve [27, 28, 29].

Several variations to the force-indentation approach exist [29, 30]. In force-volume imaging, force-indentation curves are gathered at multiple points across the sample, each point allowing for determining elasticity and adhesion. In the PeakForce quantitative nanomechanical method, the cantilever is oscillated below resonance (typically 1 kHz) with each oscillation resulting in a force-indentation curve, allowing for improved imaging speeds. Related developments perform frequency-dependent mapping of the nanomechanical properties [31]. Furthermore, some techniques have been proposed for additionally determining viscous properties from force-indentation curves by exploiting the time-history of the data [32, 33].

Early results in AFM have shown that the amplitude and phase of a dynamically excited cantilever can be mapped to both elastic and viscous properties of the sample [34]. More recently, multiharmonic approaches have been developed for mapping mechanical properties of cells [35, 36]. Here, the cantilever is typically excited at resonance frequency. As the cantilever is scanned across the sample, the measurable signals are mapped to local mechanical properties such as elasticity and viscosity. This approach allows for a considerable increase in acquisition speed.

In this article a new technique for the identification of viscoelastic properties of soft samples in AFM is presented, first developed in [37, 38]. Here, the sample is modeled as a dynamic model with unknown parameters, in terms of a laterally spaced grid of spring constants and damping coefficients. The parameters are identified from the measurable signals, using tools from the control literature. Essentially, the measurable signals are mapped to the parameters of the sample model recursively in a least squares sense, making it possible to observe changes over time. The estimated parameters are guaranteed to converge to the real values exponentially fast provided a suitable control input is chosen.

This technique can be operated in two distinct modes. In dynamic indentation viscoelastic (DIVE) mode [37], mechanical properties of the sample are identified at a discrete number of points by indenting in and out of the sample. In the scanning viscoelastic (SVE) mode [38], viscoelastic properties are gathered in a continuous fashion as the sample is scanned along the lateral axes at constant depth. In this article the two modes are expanded upon and compared.

In Section 2 a system model description of the viscoelastic sample is designed, suitable for parameter identification. The two modes of operation, DIVE and SVE, are presented in Section 3. Next, Section 4 presents the identification techniques for the unknown parameters of the system. Results are given in Section 5. In Section 6 the technique is discussed in the context of previous approaches and future considerations, and in Section 7 final conclusions are reached.

2. System Modeling

In this section, the system modeling is presented. This includes the dynamics of the sample, the cantilever dynamics, the geometry of the tip and their combinations, in order to acquire a full system description. The purpose of the modeling is to provide a description of the interaction between the cantilever and a general viscoelastic sample material, while allowing for simple identification of the model parameters by the usage of the atomic force microscope.

2.1. Sample Dynamics

The modeled sample is considered as a system of discrete spring-damper elements, as illustration in Fig. 1. The elements are evenly distributed in the lateral xy-axes, and can be compressed in the vertical z-direction [37], [38].

The interaction between the AFM cantilever and the sample is analytically presented, and illustrated in Fig. 2. The position of the tip along the xyz-axes is denoted by (X, Y, Z). The vertical tip position Z, the cantilever deflection D, and the controllable cantilever base position U are related by

$$Z = U - D. \tag{1}$$

Since the deflection D is measurable and U is controllable, all three signals are assumed to be available.

The dynamics between the cantilever and the sample can be described by three main components as seen in Fig. 3. The cantilever dynamics is subject to an external sample force which generates a deflection along the vertical axis. The tip geometry and position is then used to determine the (possibly compressed) positions of each sample spring-damper element. The compressed elements in turn

creates a restoration force acting on the cantilever tip. The details of each of these components will be described in the following.

2.2. Cantilever Dynamics

The cantilever dynamics can be approximated by its first resonance mode [39], resulting in the spring-damper system

$$M\ddot{Z} = KD + C\dot{D} + F_{\text{ts}} \tag{2}$$

where M is the effective mass of the cantilever [40], K, C are the cantilever spring and damping constants respectively, and F_{ts} is the force from the sample acting on the cantilever tip.

2.3. Tip Geometry

The cantilever tip is modeled as a sphere with tip radius R. The vertical position z_i of the spring-damper element i in contact with the tip is then given by

$$z_i = Z - \sqrt{R^2 - (X - x_i)^2 - (Y - y_i)^2} \tag{3}$$

$$\dot{z}_i = \dot{Z} \tag{4}$$

where x_i, y_i are the position of the element along the lateral axes, and $\dot{z}_i$ is the element velocity. It has been assumed that $\dot{X}$ and $\dot{Y}$ are much smaller than $\dot{Z}$. This is justified by the fact that the cantilever is oscillated at a high frequency near resonance resulting in a significant rate of change in Z, while the sample is scanned comparatively slow in the lateral directions.

A spherical tip can be advantageous in use with soft, fragile samples [41], although if desired the equations (3)-(4) can be modified to handle different tip geometries. The tip geometry is only necessary for simulation purposes, as the parameter identification scheme does not require a tip model. However, the scaling of the identified parameters are dependent on the tip. Thus, if the radius or geometry is not known, the identified values will be scaled inaccurately. However, this inaccuracy will be consistent across the sample.

2.4. Sample Force

The sample is modeled by viscoelastic elements. Thus, each element in contact with the tip provides spring and damping forces. The force from element i can be described by

$$F_i = k_i\delta_i + c_i\dot{\delta}_i \tag{5}$$

where k_i is the spring constant of element i, c_i is the damping coefficient, and δ_i is the indentation of the tip into the element,

$$\delta_i = h_i - z_i \tag{6}$$

where h_i is the rest-position of the element, or equivalently the sample height (topography) at the position of the element. The sample is assumed not to display permanent deformations. Thus, $\dot{\delta}_i = -\dot{z}_i$ since the sample height is constant.

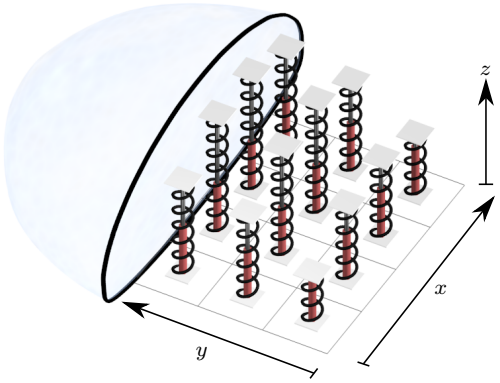

Figure 1: The sample is modeled as spring-damper elements evenly spaced along the lateral axes.

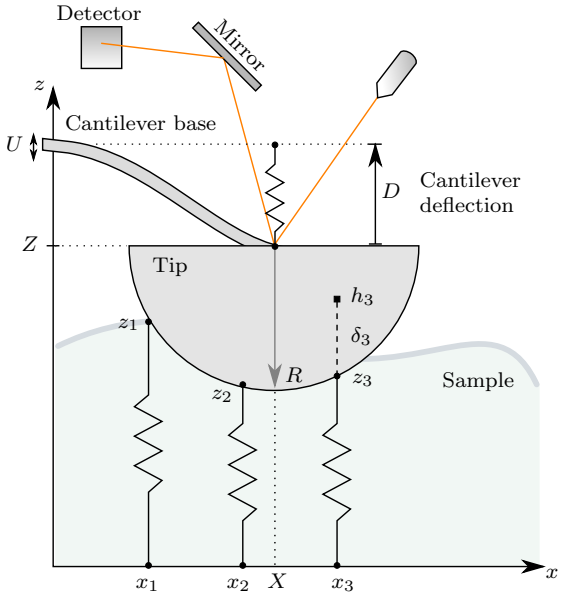

Figure 2: Indentation of the tip into the sample.

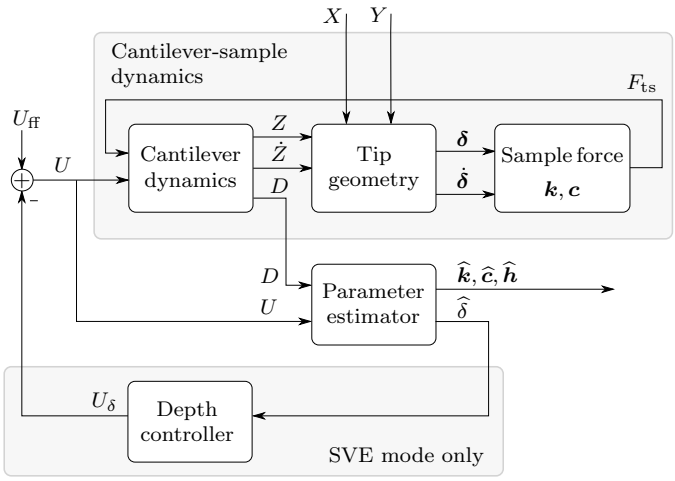

Figure 3: Block diagram of the cantilever-sample dynamics and parameter estimator. The parameter estimates are based solely on measurements of the deflection output D and the vertical position control input U.

The sample elements in contact with the tip is denoted by the active set $\mathcal{W}(X, Y, Z)$ which changes as the tip scans over the sample,

$$\mathcal{W} = \left\{ i \,:\, \delta_i > 0 \,\wedge\, (X - x_i)^2 + (Y - y_i)^2 < R^2 \right\}. \quad (7)$$

The element i is thus only added to the active set if the tip is indenting it. This method could be extended to model the attractive forces near the surface by including elements with a small negative value of δ_i.

The sum of the forces acting on the cantilever tip from the sample is then given by

$$F_{\text{ts}} = \sum_{i \in \mathcal{W}} F_i. \quad (8)$$

In the following, the vectors $\boldsymbol{k}, \boldsymbol{c}, \boldsymbol{h}$ are used to refer to the family of elements, e.g. $\boldsymbol{k} = \{k_1, ..., k_m\}$ where m is the number of spring-damper elements in the sample.

3. Modes of Operation

The modeling and identification approach described in this article can be operated in two distinct modes, both of which identify the unknown sample parameters of the dynamic sample model.

3.1. Dynamic indentation viscoelastic mode

In DIVE mode the cantilever moves across the sample surface without contact. At discrete points in space, the lateral movement is paused and the tip is lowered into the sample and identifies the sample properties at this single point. The cantilever is then raised and the procedure is repeated across the sample to form an $N \times N$ grid of identified parameters. The name should not be confused with the traditional dynamic imaging mode in AFM.

In this mode, the tip is lowered sufficiently such that the entire tip is submerged into the sample. This is not strictly necessary, although for consistent measurements the scaling of the parameters, as discussed later, would need to be revised to account for this case.

3.2. Scanning viscoelastic mode

In SVE mode the cantilever is always in contact with the sample, scanning continuously at constant depth across the surface of the sample in a raster pattern. The sample parameters are identified continuously resulting in an $N \times M$ grid of resolved parameters, where N is the number of discrete lines and M is the number of samples of the continuous signal at each line.

4. Parameter Identification

In this section it is shown how the unknown parameters of the system, $\boldsymbol{k}, \boldsymbol{c}, \boldsymbol{h}$, can be estimated. As seen in Fig. 3 the parameter estimator is separated from the system and only the cantilever deflection D and vertical control input signal U is assumed available for measurement.

4.1. Parametric system model

The system equations needs to be on a form suitable for parameter identification. Rewriting (2) and inserting for (5),(8) gives

$$M\ddot{Z} - KD - C\dot{D} = \sum_{i \in \mathcal{W}} k_i \delta_i + c_i \dot{\delta}_i \quad (9)$$

where the signals on the left hand side are known, and the right hand side contains the parameters to be estimated. It would be very challenging to determine all the sample parameters of each element individually. The problem is therefore simplified by rather trying to estimate the aggregated spring constant k and damping constant c at the current tip position. The system can thus be approximated by

$$M\ddot{Z} - KD - C\dot{D} = k\delta + c\dot{\delta} \quad (10)$$

where c, k are now slowly-varying parameters as a function of the current lateral tip position (X, Y). By continuously estimating and logging c, k as the tip is scanned or tapped across the sample, the local viscoelastic properties of the sample are determined.

The indentation depth of the tip into the sample is given by

$$\delta = h - Z \quad (11)$$

where h is the unknown sample topography at the current tip position.

In DIVE mode, the topography h can be found from a simplified approach by recording the first point of contact during a tap, thus δ is assumed known in this mode. However, in SVE mode this approach does not work because the cantilever moves in the lateral directions while being indented. Thus, the topography parameter h will change after first point of contact.

Due to the difference in assumption of known δ, the parametric system model will have to differ between the two modes.

4.1.1. DIVE mode system

The system equations (10) can be rearranged and rewritten in the complex s-domain as

$$Ms^2Z - CsD - KD = (cs + k)\,\delta \quad (12)$$

which can be formulated as

$$w'_{\text{D}} = \begin{bmatrix} c \\ k \end{bmatrix}^T \begin{bmatrix} s\delta \\ \delta \end{bmatrix} \quad (13)$$

$$= \boldsymbol{\theta}_{\text{D}}^T \boldsymbol{\phi}'_{\text{D}} \quad (14)$$

where the known w'_{D} is the left hand side of (12), $\boldsymbol{\theta}_{\text{D}}$ is the unknown parameter vector to be estimated, and $\boldsymbol{\phi}_{\text{D}}$ is the known signal vector.

4.1.2. SVE mode system

Using (10), and inserting for (1) and (11), the system equations can be rewritten as

$$Z(Ms^2 + Cs + K) - U(Cs + K) = k(h - Z) - csZ \quad (15)$$

where it has been used that h is a slowly-varying parameter, thus $\dot{h}$ can be approximated by zero. The parametric system equations can now be represented by

$$w'_{\mathrm{S}} = \begin{bmatrix} c \\ k \\ kh \end{bmatrix}^T \begin{bmatrix} -sZ \\ -Z \\ 1 \end{bmatrix} \quad (16)$$

$$= \boldsymbol{\theta}_{\mathrm{S}}^T \boldsymbol{\phi}'_{\mathrm{S}} \quad (17)$$

where w'_{S} is the left hand side of (15), and $\boldsymbol{\theta}_{\mathrm{S}}, \boldsymbol{\phi}_{\mathrm{S}}$ are the parameter and signal vector respectively.

4.1.3. Filtered system equations

In order to avoid pure differentiation of the signals in (13),(16), both sides of each equation is filtered by a second-order low-pass filter such as $1/\Lambda(s) = 1/(\lambda s + 1)^2$,

$$\frac{w'_\jmath}{\Lambda} = \boldsymbol{\theta}_\jmath^T \frac{\boldsymbol{\phi}'_\jmath}{\Lambda} \quad (18)$$

$$w_\jmath = \boldsymbol{\theta}_\jmath^T \boldsymbol{\phi}_\jmath. \quad (19)$$

for $\jmath \in \{\mathrm{D}, \mathrm{S}\}$.

This linear-in-the-parameters form is suitable for implementation of various parameter estimation methods such as given in [42]. The objective of the estimator is thus to find the unknown $\boldsymbol{\theta}_\jmath$ given the signals $w_\jmath$ and $\boldsymbol{\phi}_\jmath$.

4.2. Parameter Estimator

Several estimation methods for the system (19) can be employed with similar stability and convergence properties. We have chosen the least squares method with forgetting factor from [42]. Due to the slowly varying nature of the parameters, a forgetting factor is useful. The method is restated here for completeness,

$$\widehat{w}_\jmath = \widehat{\boldsymbol{\theta}}_\jmath^T \boldsymbol{\phi}_\jmath \quad (20)$$

$$\varepsilon_\jmath = (w_\jmath - \widehat{w}_\jmath)/m_\jmath^2 \quad (21)$$

$$m_\jmath^2 = 1 + \alpha \boldsymbol{\phi}_\jmath^T \boldsymbol{\phi}_\jmath \quad (22)$$

$$\dot{\widehat{\boldsymbol{\theta}}}_\jmath = \mathbf{P}_\jmath \varepsilon_\jmath \boldsymbol{\phi}_\jmath \quad (23)$$

$$\dot{\mathbf{P}}_\jmath = \begin{cases} \beta \mathbf{P}_\jmath - \mathbf{P}_\jmath \frac{\boldsymbol{\phi}_\jmath \boldsymbol{\phi}_\jmath^T}{m_\jmath^2} \mathbf{P}_\jmath, & \text{if } \|\mathbf{P}_\jmath\| \le R_0 \\ 0, & \text{otherwise} \end{cases} \quad (24)$$

$$\mathbf{P}_\jmath(0) = \mathbf{P}_{\jmath,0} \quad (25)$$

for $\jmath \in \{\mathrm{D}, \mathrm{S}\}$, where α, β, R_0 are positive constants, and $\mathbf{P}_{\mathrm{D}} \in \mathbb{R}^{2\times 2}, \mathbf{P}_{\mathrm{S}} \in \mathbb{R}^{3\times 3}$ are the covariance matrices.

This method guarantees convergence of the error $\varepsilon_\jmath$ to zero given constant parameters $\boldsymbol{\theta}_\jmath$ as in DIVE mode. The parameters in SVE mode are slowly-varying, but the error can be made arbitrarily small by reducing the scanning speed.

For the parameter vector $\widehat{\boldsymbol{\theta}}_\jmath$ to converge to $\boldsymbol{\theta}_\jmath$, the signal vector $\boldsymbol{\phi}_\jmath$ needs to be persistently exciting (PE). Indeed, this is a sufficient condition for exponential convergence of $\widehat{\boldsymbol{\theta}}_\jmath \to \boldsymbol{\theta}_\jmath$ [42]. The following theorem provides conditions for PE and exponential convergence in DIVE mode. Equivalent conditions can be shown in the case of SVE mode.

Theorem 1 (Persistency of excitation). *Apply the cantilever input signal*

$$U = u_0 + a \sin(\omega_0 t) \quad (26)$$

for any positive constants a, ω_0, and let the constant u_0 be small enough for the cantilever tip to be in contact with the surface, i.e. $\delta > 0, \forall\, t$. Then $\boldsymbol{\phi}_{\mathrm{D}}$ is persistently exciting (PE) and $\widehat{\boldsymbol{\theta}}_{\mathrm{D}} \to \boldsymbol{\theta}_{\mathrm{D}}$ exponentially fast.

Proof. Expand the signal vector $\boldsymbol{\phi}_{\mathrm{D}}$ such that

$$\boldsymbol{\phi}_{\mathrm{D}} = \mathbf{H}(s)\delta, \quad \mathbf{H}(s) = \begin{bmatrix} \frac{s}{(1+\lambda s)^2} \\ \frac{1}{(1+\lambda s)^2} \end{bmatrix}.$$

Define the matrix $\mathbf{A}$ such that

$$\mathbf{A}(j\omega_1, j\omega_2) \triangleq \left[\mathbf{H}(j\omega_1)\, \mathbf{H}(j\omega_2)\right] = \begin{bmatrix} \frac{j\omega_1}{(1+\lambda j\omega_1)^2} & \frac{j\omega_2}{(1+\lambda j\omega_2)^2} \\ \frac{1}{(1+\lambda j\omega_1)^2} & \frac{1}{(1+\lambda j\omega_2)^2} \end{bmatrix}.$$

Taking the determinant of $\mathbf{A}$ gives

$$|\mathbf{A}(j\omega_1, j\omega_2)| = \frac{1}{(1+\lambda j\omega_1)^2(1+\lambda j\omega_2)^2}(j\omega_1 - j\omega_2)$$
$$\neq 0 \,\forall\, \{\omega_1, \omega_2 \in \mathbb{R} \,:\, \omega_1 \neq \omega_2\}.$$

Thus $\mathbf{H}(j\omega_1), \mathbf{H}(j\omega_2)$ are linearly independent on $\mathbb{C}^2$ $\forall\, \{\omega_1, \omega_2 \in \mathbb{R} \,:\, \omega_1 \neq \omega_2\}$. By Theorem 5.2.1 in [42] $\boldsymbol{\phi}_{\mathrm{D}}$ is then PE if and only if δ is sufficiently rich of order 2.

By Definition 5.2.1 in [42] the signal $U = u_0 + a\sin(\omega_0 t)$ is sufficiently rich of order 2. The transformation from U to δ is seen to be linear and stable by considering (1),(11),(12), which means that a sinusoidal input on U results in a sinusoidal output on δ with amplitude $\left|\frac{\delta}{U}(j\omega_0)\right|$, phase $\angle\frac{\delta}{U}(j\omega_0)$ and frequency ω_0. The signal δ is thus sufficiently rich of order 2. Thus, $\boldsymbol{\phi}_{\mathrm{D}}$ is PE. Additionally, $\boldsymbol{\phi}_{\mathrm{D}}$ is bounded since $\dot{U}$ is bounded and $\mathbf{H}(s)$, $\frac{\delta}{U}(s)$ are stable. Then, by Corollary 4.3.1 in [42] the parameter vector $\widehat{\boldsymbol{\theta}}_{\mathrm{D}} \to \boldsymbol{\theta}_{\mathrm{D}}$ exponentially fast. □

Although exponential convergence of $\widehat{\boldsymbol{\theta}}_{\mathrm{D}} \to \boldsymbol{\theta}_{\mathrm{D}}$ is guaranteed, some error is expected in the identified parameters at a given point because of the model approximation from (9) to (10).

4.3. Indentation Depth and Topography

As discussed earlier in this section, the two modes differ in how the identified topography $\hat{h}$ is found. However, for each mode, when $\hat{h}$ is found, the depth is given by

$$\hat{\delta} = \hat{h} - Z. \tag{27}$$

In the following, identification of the topography is described for each mode.

4.3.1. DIVE mode

In the identification scheme for DIVE mode, the depth was assumed known in (12). This signal can be generated by identifying $\hat{h}$ at each tap and using (27) during the tap. The procedure is described in the following.

As the tip enters the sample the cantilever will start to deflect. This point is recorded and used as the topography estimate $\hat{h}$ at the current tip position. The topography estimate is stored after each tap ℓ, generating the estimate of the complete sample topography $\hat{h}_\ell \,\forall\, \ell$. Additionally, a low-pass filter G_{lp} for attenuation of measurement noise and a hysteresis loop for avoiding retriggering during sample penetration is used in the implementation. The procedure is summarized as follows:

- Record the time $t_1 = t$ at rising edge of the boolean signal $G_{lp}D < -\gamma$, for some positive constant γ.
- Create a hysteresis loop for t_1 by disabling retriggering until $G_{lp}D < -\gamma_+$ where $\gamma_+ > \gamma$.
- Then $\hat{h} = Z(t_1)$ and $\hat{\delta}(t) = \hat{h} - Z(t)$, where as previously $Z(t) = U(t) - D(t)$.
- Store $\hat{h}_\ell = \hat{h}$ for the current tap ℓ.

4.3.2. SVE mode

In SVE mode, the topography is estimated as part of the identification scheme as seen in (16). The topography $\hat{h}$ is found after division by $\hat{k}$ in $\widehat{\theta}_{\mathrm{S},3}$. As such, the estimator should make sure $\hat{k}$ does not become zero. Since k is known to be strictly positive, a projection function such as from [43] can be used in the update law (23) to ensure $\hat{k}$ stays within provided limits.

4.4. Depth controller

In SVE mode, an additional depth controller is required. Due to the spherical nature of the tip geometry, the submerged parts of the tip into the sample will vary based on the depth of the tip. The spring and damping forces are effectively nonlinear functions of depth. Thus, constant depth is necessary in order to enforce consistent measurements across the sample. For this reason a depth controller has been designed.

A simple I-controller is used to maintain desired depth δ_{ref}, given by

$$U_\delta = k_i \int_0^t \left(\delta_{\mathrm{ref}} - \hat{\delta}(\tau)\right) d\tau. \tag{28}$$

This signal is applied to the system according to Fig. 3.

Note that due to the soft, heterogeneous sample material, traditional scanning approaches such as AM-mode is not sufficient for constant depth. This is because the varying spring and damping parameters will ultimately affect the amplitude response of the cantilever. Thus, by controlling for constant amplitude, changes in the material properties is indistinguishable from changes in depth. This would ultimately lead to errors in the identified parameters.

5. Simulation Results

5.1. Setup

Simulations have been setup according to Fig. 3 for the DIVE and SVE modes respectively. The cantilever dynamics and sample properties are identical in both modes for the purpose of comparing the results.

The sample properties have been defined over a grid of $5\,\mu\mathrm{m} \times 5\,\mu\mathrm{m}$ with 50×50 evenly spaced elements. The number of grid elements determines the smoothness of the force versus depth-response of the cantilever as it indents the sample. A high number gives a smooth curve, while a low number gives a piecewise linear approximation to the curve. On the other hand, a high number of elements is more computationally demanding. The 50×50 grid results in a fairly smooth curve as seen in Fig. 9 at reasonable computation times. The number of elements should be scaled by the area the cantilever tip covers for consistent results.

Each grid element i is represented by its topography h_i, damping coefficient c_i, and spring constant k_i. The given sample properties plotted over the spatial domain can be seen in Figs. 4a, 5a and 6a respectively. The properties have been designed to resemble a cell, but could represent any soft sample material.

A cantilever with a resonance frequency of 20 kHz was chosen with a spring constant 0.18 N/m, a damping coefficient 1.48×10^{-8} Ns/m, an effective mass 1.18×10^{-11} kg, and tip a radius 300 nm. This equates to a quality (Q) factor of 100.

DIVE mode was setup to perform a total of 20×20 indentations evenly spaced across the grid, with 0.2 s spent during each indentation for a total imaging time of 80 s. The sample parameters were recorded once towards the end of each tap.

In SVE mode, a total of 20 scanlines were performed across the sample, with a periodicity of 2 s for a total imaging time of 40 s. The sample properties were continuously sampled across the fast scanning direction, and resampled in post-processing to generate a 50×20 resolution image. A horizontal resolution of 50 was chosen to correspond to the number of defined elements. Due to phase-lag of the parameter identification scheme, the values across a backward and forward scan were averaged. Otherwise each consecutive line would appear slightly offset from the previous line.

Although the input signal from (26) is sufficient for PE conditions, the following excitation signal was implemented for both modes,

$$U_{exc} = u_0 + a_1 \sin(f_1 2\pi t) + a_2 \sin(f_2 2\pi t) \tag{29}$$

where u_0, a_1, a_2 are suitably chosen constants, f_1 is near resonance frequency of the cantilever, and f_2 is below resonance frequency. The last term is used to provide additional excitation of the signal vector for faster parameter convergence.

In DIVE mode, the excitation amplitudes a_1, a_2 were set to oscillate the cantilever tip with amplitudes of 100 nm and 25 nm respectively. The total vertical positioning signal is then given by $U = U_{exc} + U_{in}$, where U_{in} is a repeated signal actually performing the indentation.

In SVE mode, small oscillation amplitudes are used. This avoids exciting the nonlinearities of the interaction force arising due to the spherical tip geometry. Additionally, in the case of lateral friction (not implemented) the tip would more easily move across the surface. The amplitudes a_1, a_2 in this case are set to oscillate the cantilever at 5 nm and 8 nm respectively. The reference depth δ_{ref} for the feedback controller is set to 150 nm. The input signal in this mode is given by $U = U_{exc} + U_\delta$.

5.2. Scaling the parameters

The identified spring and damping constants are aggregate parameters, that is, they are the sum of the individual spring-damper elements which the tip is in contact with. Thus, they need to be scaled by the number of elements the tip covers. That is, the corrected parameters are given by

$$\hat{k}_c = \hat{k}/n, \tag{30}$$

$$\hat{c}_c = \hat{c}/n. \tag{31}$$

where $n = |\mathcal{W}|$ is the number of elements in the set $\mathcal{W}$, or equivalently, the number of sample elements the tip is in contact with.

Additionally, the non-flat tip geometry means that the indentation of individual elements will vary across the tip, even in the case of flat topography. Ultimately, this will affect the measurements of the spring constants.

In SVE mode only a small part of the tip is submerged. Thus, the error due to the spherical tip geometry is small. Additionally, due to the constant depth the error is consistent across the sample. For these reasons, the spring constant has been left uncorrected.

On the other hand, in DIVE mode the tip is completely submerged and the depth varies between each tap. In this case, the corrected spring constant is found given a completely submerged spherical tip,

$$\hat{k}_{c,\mathrm{D}} = \hat{k}_c \frac{\hat{\delta}}{\hat{\delta} - \frac{1}{3}R} \tag{32}$$

arrived at in Appendix A.

These corrections as discussed have been applied to the results. The subscripts of the corrected parameters have been omitted for the sake of readability.

5.3. Results

Comparison of the identified topography for each mode to the given topography is seen in Fig. 4. The identified damping coefficients are seen in Fig. 5, and the identified spring constants are given in Fig. 6.

The error plots of the identified properties are given in Fig. 7. The errors are given in percentages of the maximum value of each property, that is, $h_{max} = 0.3\,\mu\text{m}$, $c_{max} = 8 \times 10^{-7}\,\text{Ns/m}$, and $k_{max} = 5 \times 10^{-3}\,\text{N/m}$ respectively.

In general, it is seen that both modes quite accurately represent the real sample properties. The real properties have small details that are not captured by any of the operating modes. This is expected for two reasons:

1. The large tip radius covers several sample elements essentially acting as an averaging filter. Details smaller than the radius will be less distinguishable.
2. The resolution is essentially limited by the number of indentations (DIVE mode) or scanlines (SVE mode), thus obfuscating high-resolution details.

From the error plots it can be seen that in general the errors are larger in the cases where the topography gradient is large. This effect and other biases are discussed in Appendix B.

Fig. 8 demonstrates the differences between the two modes of operation. For each mode it is seen how the parameter identification scheme approaches the real values across a complete cross section of the sample. Additionally, the vertical positioning input U is plotted to further demonstrate the differences between the modes.

The parameters presented in Fig. 8b experience a high-frequency oscillation. This is possibly due to the forced high-frequency oscillation of the cantilever, possibly combined with high gains in the parameter estimator. The frequencies are higher than the horizontal resolution of the image and the number of defined elements, thus the oscillations are not visible after resampling and anti-aliasing.

6. Discussion

6.1. Comparison to existing techniques

6.1.1. Sample modeling

The modeling approach presented in this article should be examined to evaluate how it compares to previous experiments. In traditional Hertzian contact models the indentation depth is correlated to the loading force F_k by $F_k \propto \delta^{1.5}$ for a spherical indenter. Experiments have shown exponents ranging between 1.5 and 2.0 depending on the bluntness of the tip [44]. In Fig. 9 it is seen that during an indentation in our model the exponent is 1.72 which fits well within the range of previous experiments.

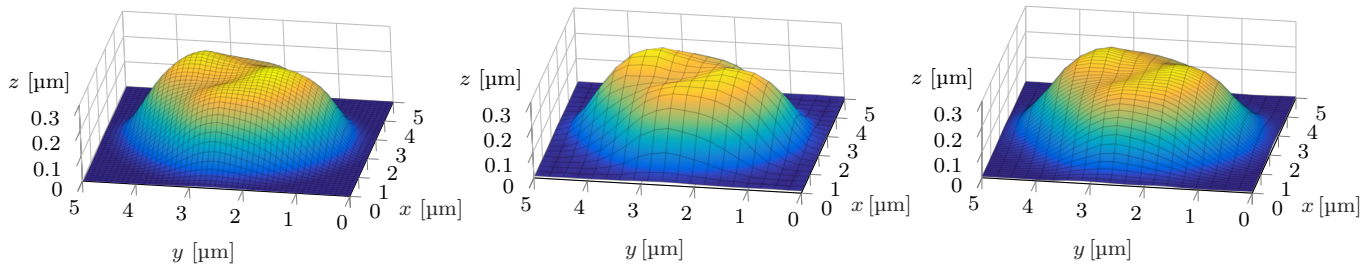

(a) Given values, $\boldsymbol{h}$ (b) DIVE mode, $\widehat{\boldsymbol{h}}_{\mathrm{D}}$ (c) SVE mode, $\widehat{\boldsymbol{h}}_{\mathrm{S}}$

Figure 4: Sample topography (a), versus identified topography (b)-(c).

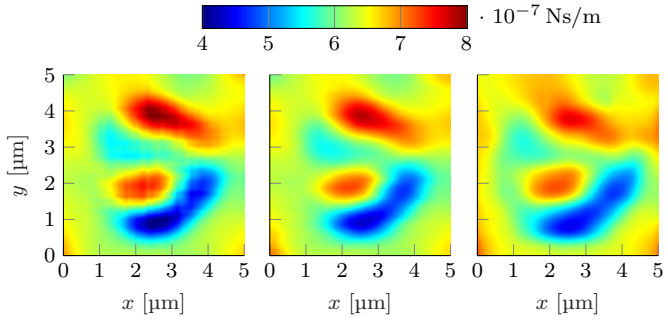

(a) Given values, $\boldsymbol{c}$ (b) DIVE, $\widehat{\boldsymbol{c}}_{\mathrm{D}}$ (c) SVE, $\widehat{\boldsymbol{c}}_{\mathrm{S}}$

Figure 5: Sample viscosity (a), versus identified viscosity (b)-(c).

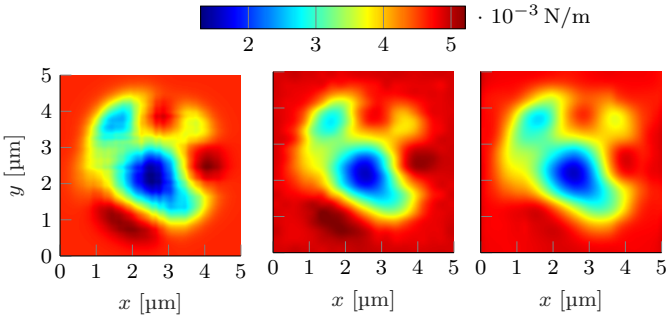

(a) Given values, $\boldsymbol{k}$ (b) DIVE, $\widehat{\boldsymbol{k}}_{\mathrm{D}}$ (c) SVE, $\widehat{\boldsymbol{k}}_{\mathrm{S}}$

Figure 6: Sample elasticity (a), versus identified elasticity (b)-(c).

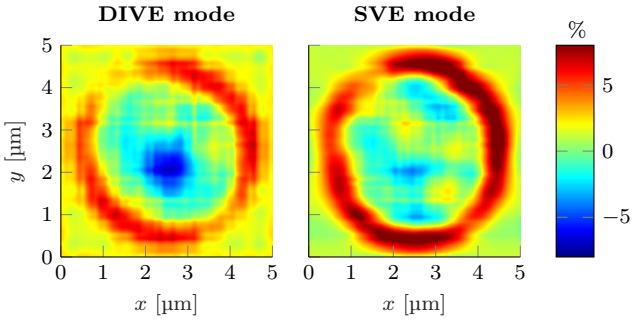

(a) Topography, $\widehat{\boldsymbol{h}} - \boldsymbol{h}$

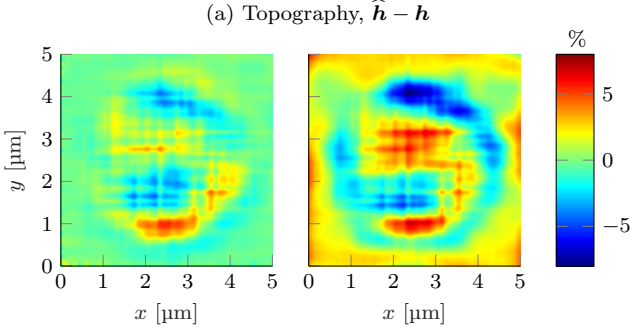

(b) Viscosity, $\widehat{\boldsymbol{c}} - \boldsymbol{c}$

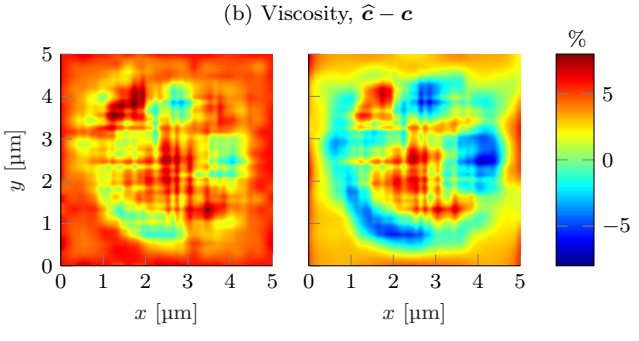

(c) Elasticity, $\widehat{\boldsymbol{k}} - \boldsymbol{k}$

Figure 7: Error plots of identified parameters.

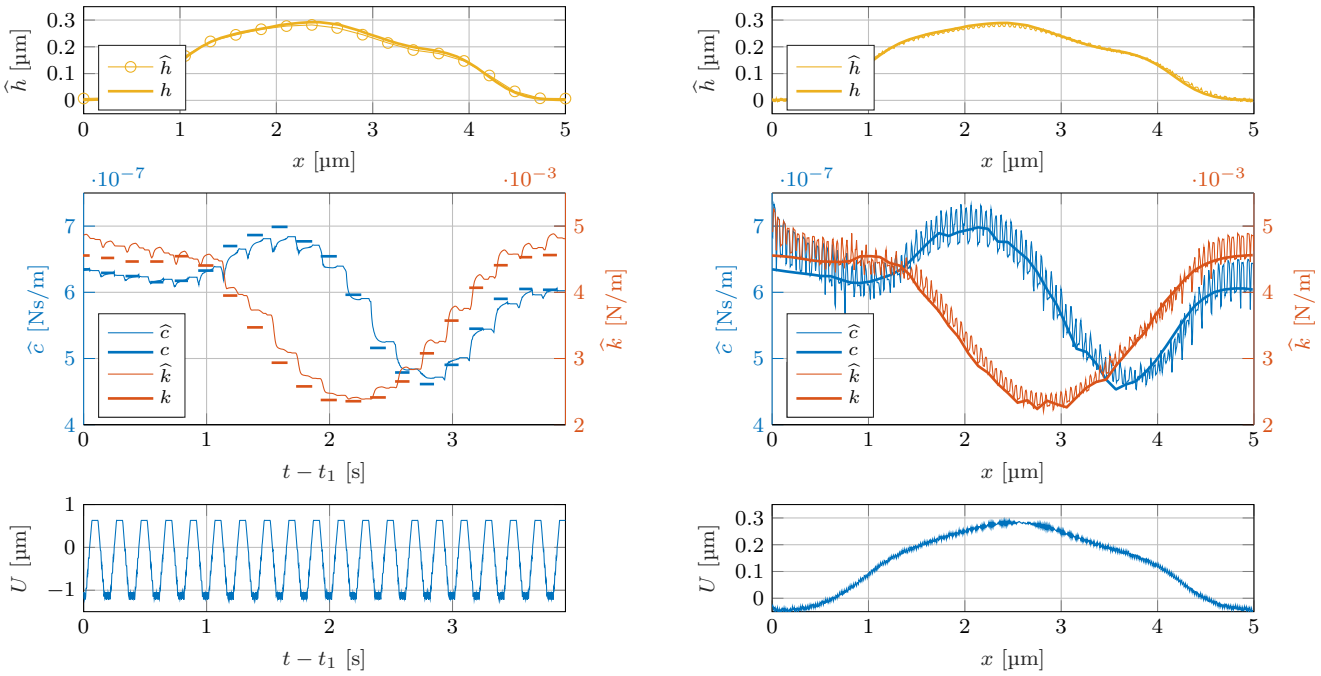

(a) DIVE mode

(b) SVE mode

Figure 8: Convergence of the identified parameters along the sample cross section at $y = 0.158\,\mu m$. In DIVE mode (a) lateral positioning of the tip pauses during each indentation, thus the properties are shown in the time domain. In SVE mode (b) the lateral tip speed is constant, thus all plots can be mapped to the spatial domain.

Although classical Hertzian contact mechanics seems to correlate well with experimental observations [25], it is based on some inherently strong assumptions. This includes small strains (indentations), homogeneous sample elasticity, and frictionless surfaces [45, 41]. The model presented in this paper however is not inherently restricted by these limitations, or is easily extendable to account for them.

- Longer indentation ranges can be accounted for, e.g. by introducing nonlinear springs.
- The presented model allows for local variations in the elasticity at any spatial resolution.
- Friction can easily be added to the model by forces.

In static Hertzian contact mechanics identifying dynamic phenomena such as damping is not possible or relevant. Since our presented model is dynamic in nature, such phenomena appear effortlessly in the model. Other dynamic phenomena can also be included in the model such as plasticity and hysteresis [46]. However, this will require some additional effort for identifying the relevant parameters.

6.1.2. Identification of mechanical properties

Recently, approaches based on multiharmonic AFM have become increasingly popular. In these approaches, the harmonic components of the cantilever's response to interaction with the sample surface is mapped to the mechanical properties of the sample. Typically, the 0th, 1st, and 2nd harmonics are used for mapping elasticity and viscosity. The operation of the SVE mode is related to the multiharmonic technique. Both approaches scans across the surface at some indentation level with forced oscillations. However, the differences are clear when it comes to mapping the measured signals to mechanical properties. The multiharmonic approach evaluates several of the first few Fourier coefficients of the conservative and dissipative parts of the tip-sample interaction force. Then, these coefficients are mapped to local material properties through a Taylor expansion of the interaction force around the indentation point [35].

Instead, in both modes presented in this article, the measured signals are mapped to a dynamic model of the sample in a least square sense, using traditional parameter estimation techniques from the control literature. This approach has several advantages:

1. The sample model can easily be extended for measurements of additional sample properties. Even certain nonlinearities can easily be implemented in the sample model and parameter estimator.
2. Errors in the dynamic model after mapping the parameters can easily be seen. This allows the user to see how well the measured properties matches the reality of the physical sample. Furthermore, these errors can be used to improve the model in an iterative approach, possibly using a data-driven modeling ap-

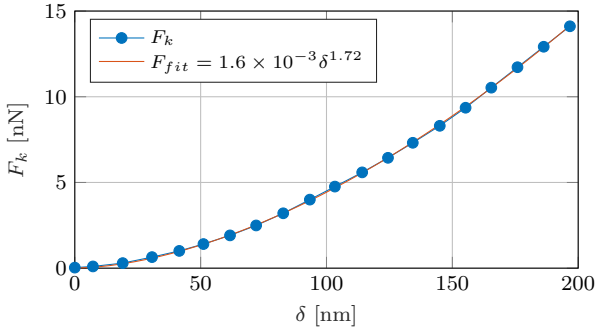

Figure 9: Spring force over depth during indentation.

proach.

3. Such a dynamic model allows for predictive behavior of the material, and, it can be argued, leads to a more intuitive description of how the sample behaves.

DIVE mode can be considered a hybrid between the SVE mode and force-volume imaging. It is similar to the latter in how it indents into the sample at discrete points along the lateral axes. However, it retains the advantages of SVE mode as it excites the sample at higher frequencies and exploits this for measuring dynamic properties of the sample.

6.2. DIVE mode versus SVE mode

The two modes of operation are both shown to be feasible candidates for identifying mechanical properties of a soft sample. However, there are certain differences between the two modes that should be emphasized.

DIVE mode indents deeper into the sample and assumes a completely submerged tip. However, with revised scaling of the parameters this mode could also tap at smaller indentation ranges. The pixel throughput of the two modes favors the SVE method with twice the number of pixels at half the time.

Earlier studies have demonstrated a difference between elasticity measurements in traditional F-Z curves and more recent multiharmonic techniques, by up to an order of magnitude [35]. Materials such as cells can display variable elasticity and possibly damping as a function of both depth and frequency. Due to the differences in indentation depth and operation of the two modes in this article, they may essentially measure different physical properties of the sample. As such, the modes supplement each other.

In SVE mode, an additional depth controller was proposed. This controller has a potential of replacing the traditional amplitude estimation feedback when scanning soft materials. The viscoelastic measurements are known to change with depth. By scanning at constant depth, consistency of the results is maintained.

6.3. Implementability for experiments

For experimental implementation only the parameter estimator needs to be considered. The sample modeling part does not need to be considered, as its primary purpose is to provide a foundation for design and analysis of the parameter estimator, as well as simulation implementations.

Some complications may arise during experiments. DIVE mode registers the height at the first point of contact, but some materials may not have a clearly defined edge, i.e. h, because of varying and possibly attractive tip-sample forces near the surface. If such forces are different between indentation points it may influence the measurements, especially for topography and spring constants.

The DIVE mode assumes a completely submerged tip. Depending on the softness and properties of the material being investigated, this may induce large stresses and possibly permanently deform the sample. A possible solution is to reduce the indentation depth and scale the measured parameters accordingly.

DIVE mode should be simple to implement because only a feedforward signal needs to be implemented online. The parameter estimator can be run offline as a post-processing technique of the measured signals. However, in SVE mode, the parameter estimator is used for depth estimation and feedback control. Thus, at least parts of the parameter estimator needs to run online. If issues arise due to online implementability, the complexity of the solution could be reduced by implementing the pre-filters for $\widehat{\phi}$ and $\widehat{w}$ in analog circuitry and use the gradient method [42] for the parameter estimation. This would reduce the digital implementation to a few arithmetic operations plus an integrator, in addition to the I-controller.

7. Conclusion

A new technique based on modeling and parameter estimation for simultaneously identifying the topography, damping coefficients, and spring constants of soft samples has been presented. The technique can be operated in two distinct modes, both of which share advantages over existing approaches. The advantages of such a modeling and identification approach include: (1) easily allowing extensions to account for additional physical phenomena such as nonlinear springs, (2) iterability of the sample model to correct for modeling errors visible in measured data, and (3) allowing the behavior of the material to be predicted through simulations of the obtained dynamic model, such as after experiments.

The two modes of operation, DIVE- and SVE mode, are compared and evaluated. Both modes are shown to be feasible in simulation studies, and they could supplement each other in experiments. DIVE mode may be easier to implement due to its lack of feedback signal. However, SVE mode displays a faster pixel throughput.

Appendix A. Corrected Spring Constant

The indentation of the tip into the sample, δ, is defined as the distance from the edge of the tip to the surface. However, the indentation of each sample element δ_i

is smaller or equal to δ as seen in Fig. A.1. This creates a discrepancy between the sum of the spring force of each element, and the spring force identified in the approximated model for parameter identification. In the following, it is shown how to correct for this discrepancy.

Assuming homogeneous spring constants, $k_i \equiv k_0$, and completely submerged tip as in DIVE mode, $\delta \geq R$. From (5),(8) the total spring force acting on the tip is then given by

$$F_k = \sum_i k_0 \delta_i = k\delta \tag{A.1}$$

where k is the aggregate spring constant from the approximated model (10), and δ from (11) is the depth into the sample measured at the end of the tip. The scaling between k_0 and k can then be found as

$$\begin{aligned} k_0 &= \frac{\delta}{\sum_i \delta_i} k \\ &= \frac{\delta}{n\delta - (\sum_i \delta - \delta_i)} k \end{aligned} \tag{A.2}$$

where $n = |\mathcal{W}|$ is the number of elements under the tip. An expression for the summation term can be found by considering the spherical tip geometry:

$$\begin{aligned} \frac{1}{n}\sum_i \delta - \delta_i &= R - \frac{1}{n}\sum_i \sqrt{R^2 - (X - x_i)^2 - (Y - y_i)^2} \\ &\approx R - \frac{1}{\pi R^2}\int_0^{2\pi}\int_0^R \rho\sqrt{R^2 - \rho^2}\, d\rho d\theta \\ &= R - \frac{2}{3}R \\ &= \frac{1}{3}R. \end{aligned} \tag{A.3}$$

The only approximation is due to moving from the discrete case to the continuous case. Inserting the last line into (A.2) gives

$$k_0 \approx \frac{1}{n}\frac{\delta}{\delta - \frac{1}{3}R} k$$

Since k and δ are not available, they can be replaced by their identified versions. In summary, the corrected spring constant for a completely submerged tip is given by

$$\hat{k}_c = \frac{1}{n}\frac{\hat{\delta}}{\hat{\delta} - \frac{1}{3}R}\hat{k} \tag{A.4}$$

Appendix B. Sources of Error

Some errors in the measured topography, viscosity, and elasticity can be explained by considering how the tip intersects with a sample of varying topography, see Fig. B.2. A flat topography is the ideal case, in which the measured and actual height is equivalent.

When the tip is placed over the highest point of a concave topography, the measured height will be correct.

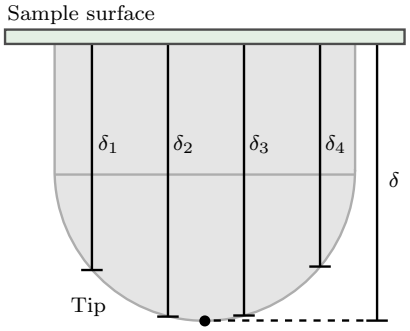

Figure A.1: The indentation depth δ is larger than the average of the element depths, δ_i. This introduces a bias in the identified spring constant, which can be corrected for in post-processing.

However, since the submerged volume of the tip is smaller than in the ideal case, an error will be introduced in the measured viscosity and elasticity.

Lastly, in the case of steep topography, the side of the tip will touch the sample first. Additionally, only small parts of the tip will be submerged as the tip descends. This introduces errors in measured topography (ε_h), elasticity, and viscosity.

These errors can be mitigated by using a tip with a smaller radius. Additionally, the errors will be reduced when the gradient of the sample topography is smaller.

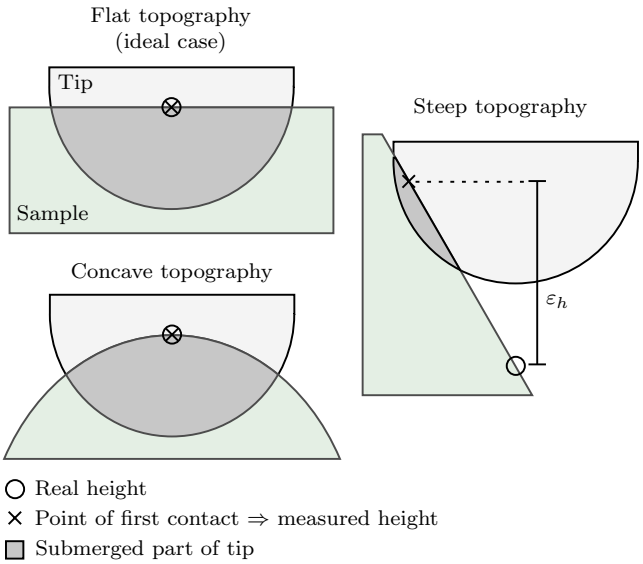

Figure B.2: Errors due to varying topography.

References

[1] N. Vahabi S., Bahareh, A. Janvanmard, Atomic Force Microscopy Applications in Biological Research: A Review Study, Iranian Journal of Medical Sciences (2013) 16–83.

[2] S. Gould, O. Marti, B. Drake, L. Hellemans, C. E. Bracker, P. K. Hansma, N. L. Keder, M. M. Eddy, G. D. Stucky, Molecular resolution images of amino acid crystals with the atomic force microscope, Nature 332 (6162) (1988) 332–334.

[3] B. Rateesh, S. Esmita, Atomic Force Microscopy: A Source of Investigation in Biomedicine, International Journal of Electronic and Electrical Engineering 11 (23) (2014) 4553–4732.
[4] T. Uchihashi, H. Watanabe, S. Fukuda, M. Shibata, T. Ando, Functional extension of high-speed AFM for wider biological applications, Ultramicroscopy 160 (2016) 182–196.
[5] I. Sokolov, Atomic Force Microscopy in Cancer Cell Research, Cancer Nanotechnology 1 (2007) 1–17.
[6] M. Lekka, K. Pogoda, J. Gostek, O. Klymenko, S. Prauzner-Bechicki, J. Wiltowska-Zuber, J. Jaczewska, J. Lekki, Z. Stachura, Cancer cell recognition – Mechanical phenotype, Micron 43 (12) (2012) 1259–1266.
[7] D. E. Discher, D. H. Boal, S. K. Boey, Simulations of the erythrocyte cytoskeleton at large deformation. II. Micropipette aspiration., Biophysics 75 (3) (2008) 1584–1597.
[8] A. R. Bausch, F. Ziemann, A. A. Boulbitch, K. Jacobson, E. Sackman, Local measurements of viscoelastic parameters of adherent cell surfaces by magnetic bead microrheometry, Biophysics 75 (4) (1998) 2038–2049.
[9] J. Guck, R. Ananthakrishnan, C. C. Cuningham, J. Kas, Stretching biological cells with light, Journal of Physics: Condensed Matter 14 (19) (2002) 4843–4856.
[10] F. M. Hecht, J. Rheinlaender, N. Schierbaum, W. H. Goldmann, B. Fabry, T. E. Schaffer, Imaging viscoelastic properties of live cells by AFM: power law rheology on the nanoscale, Soft matter 7 (1) (2015) 59–66.
[11] G. Schitter, K. J. Astrom, B. E. DeMartini, P. J. Thurner, K. L. Turner, P. K. Hansma, Design and modeling of a high-speed AFM-scanner, Control Systems Technology, IEEE Transactions on 15 (5) (2007) 906–915.
[12] Y. K. Yong, S. S. Aphale, S. O. R. Moheimani, Design, identification, and control of a flexure-based XY stage for fast nanoscale positioning, IEEE Transactions on Nanotechnology 8 (1) (2009) 46–54.
[13] A. J. Fleming, S. S. Aphale, S. O. R. Moheimani, A New Method for Robust Damping and Tracking Control of Scanning Probe Microscope Positioning Stages, IEEE Transactions on Nanotechnology 9 (4) (2010) 438–448.
[14] R. Garcia, E. T. Herruzo, The emergence of multifrequency force microscopy, Nature Nanotechnology 7 (4) (2012) 217–226.
[15] M. Vagia, A. A. Eielsen, J. T. Gravdahl, K. Y. Pettersen, Design of a Nonlinear Damping Control Scheme for Nanopositioning, in: IEEE/ASME International Conference on Advanced Intelligent Mechatronics, 2013, pp. 94–99.
[16] M. Vagia, A. A. Eielsen, J. T. Gravdahl, K. Y. Pettersen, Nonlinear tracking control scheme for a nanopositioner, in: 24th Mediterranean Conference on Control and Automation, 2016, pp. 860–865.
[17] M. R. P. Ragazzon, J. T. Gravdahl, K. Y. Pettersen, A. A. Eielsen, Topography and force imaging in atomic force microscopy by state and parameter estimation, in: American Control Conference, Chicago, USA, 2015, pp. 3496–3502.
[18] M. R. P. Ragazzon, M. G. Ruppert, D. M. Harcombe, A. J. Fleming, J. T. Gravdahl, Lyapunov Estimator for High-Speed Demodulation in Dynamic Mode Atomic Force Microscopy, IEEE Transactions on Control Systems Technology PP (99) (2017) 1–8.
[19] M. Lekka, D. Gil, K. Pogoda, J. Dulinska-Liewka, R. Jach, J. Gostek, O. Klymenko, S. Prauzner-Bechicki, Z. Stachura, J. Wiltowska-Zuber, K. Okon, P. Laidler, Cancer cell detection in tissue sections using AFM, Archives of Biochemistry and Biophysics 518 (2) (2012) 151–156.
[20] M. Lekka, Atomic force microscopy: A tip for diagnosing cancer, Nature nanotechnology 7 (11) (2012) 691–2.
[21] R. Benitez, J. Toca-Herrera, Looking at Cell Mechanics with Atomic Force Microscopy: Experimental and Theory, Microscopy Research and Technique 77 (11) (2014) 947–958.
[22] E. Dimitriadis, F. Horkay, J. Maresca, B. Kachar, R. Chadwick, Determination of Elastic Moduli of Thin Layers of Soft Material Using the Atomic Force Microscope, Biophysical Journal 82 (5) (2002) 2798–2810.
[23] T. Uchihashi, H. Watanabe, S. Fukuda, M. Shibata, Functional extension of high speed AFM for wider biological applications, Ultramicroscopy (2016) 182–196.
[24] M. Plodinec, M. Loparic, C. A. Monnier, E. C. Obermann, R. Zanetti-Dallenbach, P. Oertle, J. T. Hyotyla, U. Aebi, M. Bentires-Alj, R. Y. H. Lim, C.-A. Schoenenberger, The nanomechanical signature of breast cancer, Nature Nanotechnology 7 (11) (2012) 757–765.
[25] T. G. Kuznetsova, M. N. Starodubtseva, N. I. Yegorenkov, S. A. Chizhik, R. I. Zhdanov, Atomic force microscopy probing of cell elasticity, Micron 38 (8) (2007) 824–833.
[26] C. T. McKee, J. A. Last, P. Russell, C. J. Murphy, Indentation versus tensile measurements of Young's modulus for soft biological tissues., Tissue engineering. Part B, Reviews 17 (3) (2011) 155–164.
[27] X. Zhu, E. Siamantouras, K. K. Liu, X. Liu, Determination of work of adhesion of biological cell under AFM bead indentation, Journal of the Mechanical Behavior of Biomedical Materials 56 (2016) 77–86.
[28] Y. M. Efremov, D. V. Bagrov, M. P. Kirpichnikov, K. V. Shaitan, Application of the Johnson-Kendall-Roberts model in AFM-based mechanical measurements on cells and gel., Colloids and Surfaces B: Biointerfaces 134 (2015) 131–139.
[29] K. K. M. Sweers, M. L. Bennink, V. Subramaniam, Nanomechanical properties of single amyloid fibrils, Journal of Physics: Condensed Matter 24 (24) (2012) 243101.
[30] M. E. Dokukin, I. Sokolov, Quantitative Mapping of the Elastic Modulus of Soft Materials with HarmoniX and PeakForce QNM AFM Modes, Langmuir 28 (46) (2012) 16060–16071.
[31] T. Li, Q. Zou, Simultaneous Topography Imaging and Broadband Nanomechanical Property Mapping using Atomic Force Microscope, in: American Control Conference, Seattle, USA, 2017, pp. 795–800.
[32] B. R. Brückner, H. Nöding, A. Janshoff, Viscoelastic Properties of Confluent MDCK II Cells Obtained from Force Cycle Experiments, Biophysical Journal 112 (4) (2017) 724–735.
[33] Y. M. Efremov, W.-H. Wang, S. D. Hardy, R. L. Geahlen, A. Raman, Measuring nanoscale viscoelastic parameters of cells directly from AFM force-displacement curves, Scientific Reports 7 (1) (2017) 1541.
[34] M. Radmacher, R. W. Tillmann, H. E. Gaub, Imaging viscoelasticity by force modulation with the atomic force microscope., Biophysical journal 64 (3) (1993) 735–742.
[35] A. Raman, S. Trigueros, A. Cartagena, A. P. Z. Stevenson, M. Susilo, E. Nauman, S. A. Contera, Mapping nanomechanical properties of live cells using multi-harmonic atomic force microscopy., Nature nanotechnology 6 (12) (2011) 809–14.
[36] A. X. Cartagena-Rivera, W.-H. Wang, R. L. Geahlen, A. Raman, Fast, multi-frequency, and quantitative nanomechanical mapping of live cells using the atomic force microscope, Scientific Reports 5 (2015) 11692.
[37] M. R. P. Ragazzon, M. Vagia, J. T. Gravdahl, Cell Mechanics Modeling and Identification by Atomic Force Microscopy, in: 7th IFAC Symposium on Mechatronic Systems, Loughborough, UK, 2016, pp. 603–610.
[38] M. R. P. Ragazzon, J. T. Gravdahl, Imaging Topography and Viscoelastic Properties by Constant Depth Atomic Force Microscopy, in: IEEE Multi-Conference on Systems and Control, Buenos Aires, Argentina, 2016, pp. 923–928.
[39] D. R. Sahoo, A. Sebastian, M. V. Salapaka, An ultra-fast scheme for sample-detection in dynamic-mode atomic force microscopy, in: 2004 NSTI Nanotechnology Conference and Trade Show, Vol. 3, 2004, pp. 11–14.
[40] B. Bhushan, O. Marti, Scanning Probe Microscopy - Principle of Operation, Instrumentation, and Probes, in: B. Bhushan (Ed.), Springer Handbook of Nanotechnology, Springer Berlin Heidelberg, 2010, pp. 573–617.
[41] I. Sokolov, M. E. Dokukin, N. V. Guz, Method for quantitative measurements of the elastic modulus of biological cells in AFM indentation experiments, Methods 60 (2) (2013) 202–213.
[42] P. A. Ioannou, J. Sun, Robust adaptive control, Prentice Hall,

Upper Saddle River, NJ, 1996.
[43] M. Krstic, I. Kanellakopoulos, P. Kokotovic, Nonlinear and adaptive control design, John Wiley & Sons, Inc., New York, NY, 1995.
[44] P. Carl, H. Schillers, Elasticity measurement of living cells with an atomic force microscope: Data acquisition and processing, Pflugers Archiv European Journal of Physiology 457 (2) (2008) 551–559.
[45] K. L. Johnson, Contact mechanics, Cambridge University Press, Cambridge, 1985.
[46] J. Å. Stakvik, M. R. P. Ragazzon, A. A. Eielsen, J. T. Gravdahl, On Implementation of the Preisach Model: Identification and Inversion for Hysteresis Compensation, Modeling, Identification and Control 36 (3) (2015) 133–142.